THz wave scattering by a graphene strip and a disk in the free space: integral equation analysis and surface plasmon resonances

2013 J. Opt. 15 114007

(http://iopscience.iop.org/2040-8986/15/11/114007)

IOP Publishing Journal of Optics
J. Opt. **15** (2013) 114007 (9pp) doi:10.1088/2040-8978/15/11/114007

THz wave scattering by a graphene strip and a disk in the free space: integral equation analysis and surface plasmon resonances

Mikhail V Balaban[1,2], **Olga V Shapoval**[1] **and Alexander I Nosich**[1]

[1] Institute of Radio-Physics and Electronics NASU, Kharkiv, 61085, Ukraine
[2] Institute of Radio Astronomy NASU, Kharkiv, 61002, Ukraine

E-mail: mikhail.balaban@gmail.com

Received 8 July 2013, accepted for publication 19 August 2013
Published 28 October 2013
Online at stacks.iop.org/JOpt/15/114007

Abstract
The excitation of the surface plasmon resonances on a graphene strip and a disk in free space is studied numerically as a 2D and 3D electromagnetic wave-scattering problem, respectively. The associated mathematical model is based on the Maxwell equations with resistive boundary conditions on the surface of a zero-thickness strip or disk, where the graphene electron conductivity is included as a parameter and determined from the Kubo formalism. It is shown that plasmon resonance frequencies in the terahertz range shift with variation of the chemical potential of the graphene. Far-field and near-field patterns are plotted at several resonance frequencies.

Keywords: surface plasmon resonance, wave scattering, graphene strip, graphene disk

(Some figures may appear in colour only in the online journal)

1. Introduction

Graphene is a planar one-atom-thick structured layer of carbon atoms which are arranged in a regular hexagonal pattern. Recently it has attracted the attention of the research community due to its amazing mechanical, electronic and optical properties. Graphene is also a zero bandgap semiconductor with conductivity tuned either by electrostatic or magnetostatic gating. It can support surface plasmon waves and, if patterned, resonance modes at low-THz frequencies. These properties of graphene make it a promising material for the development of ultrathin fast nanoelectronic devices [1–7]. To study electromagnetic wave scattering by a graphene object it is necessary to combine the Maxwell boundary value problem with a phenomenological model of the graphene conductivity [8]. The main challenge of such an approach is to involve a zero thickness of the scatterer into the model. This can be done by modeling graphene as an equivalent resistive surface (also called impedance surface because of the complex-valued resistivity). Then one can use various mesh-based and meshless codes for the numerical analysis of the wave scattering.

In this paper we present analytical–numerical methods to solve the scattering of electromagnetic waves by a single graphene strip and a disk in the free space and use them to study plasmon resonance excitation on these objects. We suppose that the size of each graphene scatterer (half-width of the strip and radius of the disk) is larger than 50 nm. This is because it has been experimentally demonstrated [9] that the edge effects on the graphene conductivity appear only in structures with dimensions smaller than 100 nm. Then we can disregard the edge effects on the graphene conductivity and use the electrical conductivity model developed for infinite graphene sheets. To solve the associated Maxwell boundary value problems we reduce each of them to a single or a set of integral equations (IEs). In the case of the scattering by a strip, such IE is a second-kind equation with a hyper-singular or log-singular integral operator, depending on the polarization. To reduce it to a matrix equation we use a Nystrom-type method with the Chebyshev or Gauss–Legendre high-order quadratures, respectively. In the case of a disk we reduce the problem to a set of coupled dual IEs in the spectral domain and then to a set of Fredholm second-kind IEs. Further we use a Nystrom-type discretization scheme to reduce it

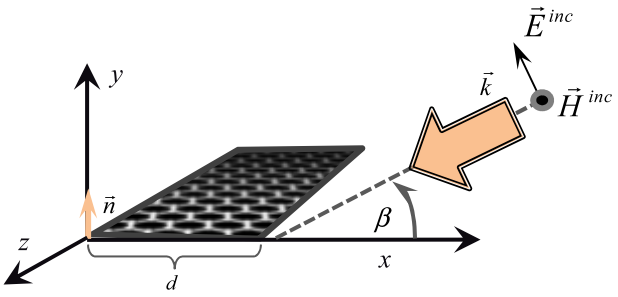

Figure 1. Micro-size graphene strip.

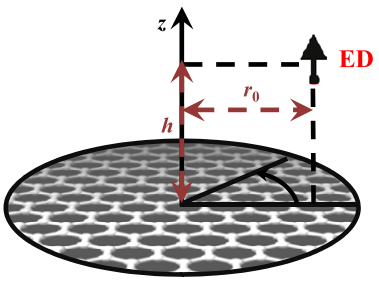

Figure 2. Micro-size graphene disk.

to a matrix equation. These numerical methods serve as a reliable instrument to study the electromagnetic response of the graphene strip and the graphene disk to the plane wave and the dipole-field excitation, respectively.

2. Problem statement

Consider two boundary value problems of the time-harmonic $[\exp(-\mathrm{i}\omega t)]$ electromagnetic field scattering by a planar graphene scatterer.

- The first is a plane H-polarized wave scattering by a graphene flat strip of the width d. Suppose that the strip stretches along the z-axis of the Cartesian coordinate system (figure 1) and β is the plane wave incidence angle measured from the x-axis.
- The second problem is the scattering of a point-source field by a graphene disk of the radius a (figure 2). Here we will consider two types of sources: vertical electrical and horizontal magnetic elementary dipoles located above the disk at the distance h and shifted from the disk axis by the distance r_0.

Decompose the total field $(\vec{E}, \vec{H})$ as a sum of the incident electromagnetic field $(\vec{E}^{\mathrm{in}}, \vec{H}^{\mathrm{in}})$ and the field scattered by the strip or the disk $(\vec{E}^{\mathrm{sc}}, \vec{H}^{\mathrm{sc}})$. Assume that the scattered field satisfies homogeneous Maxwell equations outside the scatterer, while the total field satisfies the following resistive-type boundary conditions [4–7]:

$$\begin{aligned} \left(E_{tg}^{+} + E_{tg}^{-}\right) &= 2\sigma^{-1}\vec{n} \times \left(H_{tg}^{+} - H_{tg}^{-}\right), \\ \left(E_{tg}^{+} - E_{tg}^{-}\right) &= 0. \end{aligned} \tag{1}$$

Here $\vec{n}$ is the unit vector normal to the strip or disk surface in the direction of the y-axis or z-axis, respectively, and σ is the graphene surface conductivity, which can be determined from the Kubo formalism and expressed as a sum of intraband $(\sigma_{\mathrm{intra}})$ and interband $(\sigma_{\mathrm{inter}})$ contributions given by the following expressions [3–5]:

$$\sigma_{\mathrm{intra}} = \frac{\mathrm{i}\, e^2 k_{\mathrm{B}} T}{\pi\hbar(\omega + \mathrm{i}/t_{\mathrm{relax}})} \times \left(\frac{\mu_{\mathrm{c}}}{k_{\mathrm{B}}T} + 2\ln\left[\exp\left(-\frac{\mu_{\mathrm{c}}}{k_{\mathrm{B}}T}\right) + 1\right]\right), \tag{2}$$

$$\sigma_{\mathrm{inter}} = \frac{\mathrm{i}\, e^2(\omega + \mathrm{i}/t_{\mathrm{relax}})}{\pi\hbar^2} \times \int_0^{\infty} \frac{f_{\mathrm{d}}(-\varepsilon) - f_{\mathrm{d}}(\varepsilon)}{(\omega + \mathrm{i}/t_{\mathrm{relax}})^2 - 4(\varepsilon/\hbar)^2}\, \mathrm{d}\varepsilon, \tag{3}$$

where e is the electron charge, k_{B} is the Boltzmann constant, T is the temperature, $\hbar$ is the reduced Planck constant, ω is the angular velocity, t_{relax} is the electron relaxation time, μ_{c} is the chemical potential, and f_{d} is the Fermi–Dirac distribution function.

For completeness of formulation, we request also that the total electromagnetic field satisfies the radiation condition at infinity and the condition of local integrability of power off the domain of sources, if any, and including the vicinities of strip edges and disk rim.

3. Micro-size graphene strip

3.1. Solution method: hyper-singular IE and Nystrom-type discretization

To solve the scattering problem by a flat graphene strip, we consider the 2D Helmholtz equation and resistive boundary conditions (1) on the strip surface $S = \{(x, y)\colon x \in [0, d],\ y = 0\}$. First, we take the H-polarized plane electromagnetic wave $(E_z = H_x = H_y = 0)$ as an incident field and reduce the problem to the 2D boundary value problem for the unknown scattered field function.

Suppose that $H_z(\vec{r}) = H_z^{\mathrm{sc}}(\vec{r}) + \mathrm{e}^{-\mathrm{i}k(x\cos\beta + y\sin\beta)}$ is the z-component of the total magnetic field and $H_z^{\mathrm{sc}}(\vec{r})$ is the unknown function. Here $\vec{r} = (x, y) \in \mathbb{R}^2$ is the radius vector of the observation point, and k is the free-space wavenumber. Express the unknown function as a double-layer potential,

$$H_z^{\mathrm{sc}}(\vec{r}) = \frac{\mathrm{i}}{4}\int_S w(\vec{r}) \frac{\partial H_0^{(1)}(k|\vec{r} - \vec{r}_0|)}{\partial n(\vec{r})}\, \mathrm{d}\vec{r}, \tag{4}$$

where $w(\vec{r}) = H_z^{+}(\vec{r}) - H_z^{-}(\vec{r})$ is the x-component of the electric current induced on the strip (note that in our case there is no z-component of the current) and $H_0^{(1)}(\cdot)$ is the first-kind Hankel function of zero order. Here the indices $\pm$ correspond to the limit values of the field from the top and bottom sides of the strip, respectively.

As the next step, we substitute expression (4) into the boundary conditions (1) and use the properties of the limit values of the double-layer potentials. After the introduction

of the dimensionless (normalized by the strip half-width) Cartesian coordinates (t, s), we obtain the following IE for the unknown function $w(t)$ where $t \in [-1, 1]$:

$$4(\sigma Z_0)^{-1} w(t_0) + \int_{-1}^{1} w(t) \frac{H_1^{(1)}(\chi|t-t_0|)}{|t-t_0|}\,\mathrm{d}t = f(\chi, t_0), \quad t_0 \in (-1, 1). \tag{5}$$

Here, $\chi = kd/2$ and $f(\chi, t_0) = 4\sin\beta\, \mathrm{e}^{-\mathrm{i}\chi(t_0+1)\cos\beta}$ is given by the incident field function. Note that the IE obtained is fully equivalent to the original boundary value problem [10]; this is a second-order hyper-singular equation whose integral operator should be understood in the sense of Hadamard's finite part. It is also important that in [11] it has been shown that the x-component of the electric current $w(t)$ tends to zero as a square root of the distance to the strip edge. Thus, $w(t)$ can be represented as $w(t) = \tilde{w}(t)(1-t^2)^{1/2}$, where $\tilde{w}(t)$ is a new smooth function to be found.

To solve IE (5) numerically with mathematically guaranteed convergence and hence controlled accuracy, one can use either the method of analytical regularization or the Nystrom-type discretization [12]. Here we will follow the latter approach and hence we extract the singular part of the corresponding integral operator (by analogy with [10]). After that, we discretize IE with the aid of the Chebyshev-type quadrature formula and then collocate the obtained discrete counterpart of IE (this procedure is also known as the method of discrete singularities [13] or advanced Nystrom-type method [14, 15]). As a result, we obtain the matrix equation,

$$\sum_{k=1}^{n} A_{sk}\tilde{w}(t_k) = f(\chi, t_{0s}). \tag{6}$$

Here, the matrix coefficients are defined as $(s, k = 1, \ldots, n)$

$$A_{sk} = \frac{\mathrm{i}}{\pi}\alpha_{sk} - \frac{2\mathrm{i}}{\pi\chi^2}\beta_{sk} + \frac{\pi}{(n+1)}M(\chi, t_k, t_{0s})(1-t_k^2) + 4(\sigma Z_0)^{-1}\delta_{sk}\sqrt{1-t_k^2}, \qquad Z_0 = \sqrt{\mu_0/\varepsilon_0} \tag{7}$$

$$\alpha_{sk} = -\frac{\pi}{n+1}(1-t_k^2)\left[\ln 2 + 2\sum_{l=1}^{n}\frac{T_l(t_k)T_l(t_{0s})}{l} + \frac{(-1)^k}{n+1}T_{n+1}(t_{0s})\right], \tag{8}$$

$$\beta_{sk} = \begin{cases} \dfrac{\pi}{(n+1)}\dfrac{(1-t_k^2)(1-(-1)^{k+s})}{(t_k-t_{0s})^2}, & s = k \\ -\dfrac{\pi(n+1)}{2}, & s \neq k, \end{cases}$$

where $T_l(t)$ is the Chebyshev polynomial of the second kind, δ_{sk} is the Kronecker delta, and $M(\chi, t, t_0) = \chi^{-1}H_1^{(1)}(\chi|t-t_0|)/|t-t_0| - (\mathrm{i}/\pi)\ln|t-t_0| + 2\mathrm{i}/(\pi\chi^2|t-t_0|^2)$ is the smooth function for all $t, t_0 \in [-1, 1]$. Note that here we use the same set of nulls of the second-kind Chebyshev polynomials as both the discretization nodes $\{t_k\}_{k=1,\ldots,n}$ and collocation nodes $\{t_{0s}\}_{s=1,\ldots,n}$. It is known that such reduction of IE (5) to a matrix analog (6) leads to a numerically efficient algorithm which has guaranteed and fast convergence (this follows from the convergence of the quadrature formulas) and controlled (by means of the order of interpolation used) computation accuracy [11]. After solving the matrix equation (6) numerically, we find the set of unknown function values in the node points $\{\tilde{w}(t_k)\}_{k=1,\ldots,n}$ and obtain the function $w(t)$ at the interval $[-1, 1]$ using the interpolation formula. Also note that the z-component of the magnetic field in the near- and far-zone can be expressed in terms of the unknowns,

$$H_z^{\mathrm{sc}}(\vec{r}) = \frac{\pi\mathrm{i}\chi}{4(n+1)}\sum_{s=1}^{n}\tilde{w}(t_s)(1-t_s^2)y \times \frac{H_1^{(1)}(k\sqrt{(x-d(t_s+1)/2)^2+y^2})}{\sqrt{(x-d(t_s+1)/2)^2+y^2}}, \quad \text{for all } \vec{r} = (x, y) \in \mathbb{R}^2 \setminus S, \tag{9}$$

$$H_z^{\mathrm{sc}}(\vec{r}) \underset{|\vec{r}|\to\infty}{\cong} (2/\mathrm{i}\pi k|\vec{r}|)^{1/2}\mathrm{e}^{\mathrm{i}k|\vec{r}|}\Phi(\theta), \tag{10}$$

$$\Phi(\theta) = \frac{\pi\sin\theta}{4(n+1)}\sum_{s=1}^{n} w(t_s)(1-t_s^2)\mathrm{e}^{-\mathrm{i}\chi(t_s+1)\cos\theta}, \tag{11}$$

where $\Phi(\theta)$ is the scattering pattern.

For completeness of analysis, in the alternative case of the E-polarized wave scattering ($H_z = E_x = E_y = 0$) the scattered field can be expressed as a convolution of electric current $v(\vec{r}) = \partial/\partial\vec{n}(\vec{r})[E_z^+(\vec{r}) - E_z^-(\vec{r})]$ with the Green's function, i.e. as a single-layer potential

$$E_z^{\mathrm{sc}}(\vec{r}) = \frac{\mathrm{i}k}{4}\int_S v(\vec{r})H_0^{(1)}(k|\vec{r}-\vec{r}_0|)\,\mathrm{d}\vec{r}. \tag{12}$$

Making operations similar to H-case, we obtain an IE with a logarithmic singularity in the kernel,

$$4(\sigma Z_0)^{-1}v(t_0) + \chi\int_{-1}^{1} v(t)H_0^{(1)}(\chi|t-t_0|)\,\mathrm{d}t = g(\chi, t_0), \tag{13}$$

where $g(\chi, t_0) = 4\mathrm{i}\mathrm{e}^{-\mathrm{i}\chi(t_0+1)\cos\beta}$ is given by the incident field function.

Without going into details, this IE is solved similarly to the case of H-polarization using a Nystrom-type discretization with the Gauss–Legendre quadrature formulas (for more details see [10, 14]).

3.2. Numerical results and discussion

To study the features of the plane wave scattering and absorption by a strip scatterer, the figures-of-merit are the total scattering cross-section (TSCS) and the absorption cross-section (ACS) [10]. We have studied these characteristics in the case of the normal incidence of an H-polarized plane wave on the graphene strip ($\beta = \pi/2$). Figure 3 shows the normalized by $2d$ plots of TSCS and ACS versus frequency for the strip with the width of 50 μm; the parameters of graphene are presented in the boxes.

As one can see, free-standing graphene strip demonstrates abundant number of surface plasmon resonances in the range from 1 to 10 THz. Figure 3 also shows that an increase of the chemical potential μ_c up-shifts the plasmon

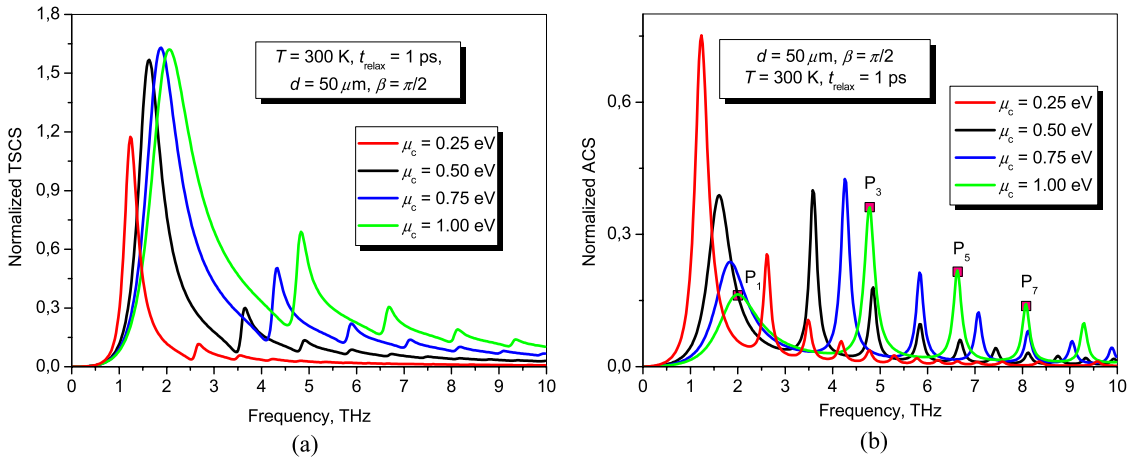

Figure 3. Normalized TSCS (a) and ACS (b) versus the frequency for the graphene strip ($d = 50\ \mu$m) illuminated by the normally incident H-polarized plane wave.

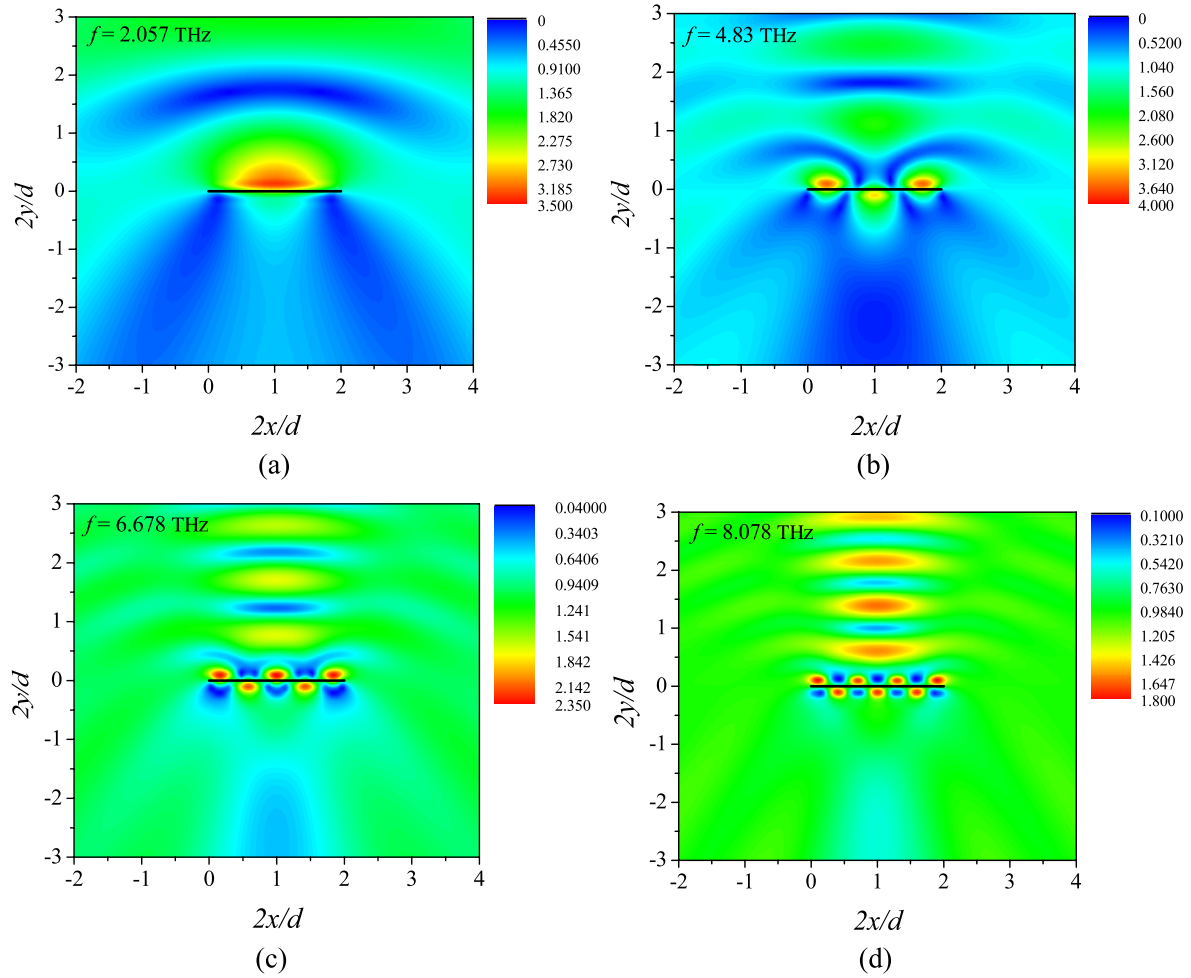

Figure 4. Total near-field patterns for a stand-alone graphene strip of $d = 50\ \mu$m at $f = 2.057$ THz (a), $f = 4.83$ THz (b), $f = 6.678$ THz (c) and $f = 8.078$ THz (d).

resonance frequencies and boosts their quality factors, which is explained by the smaller losses in graphene.

More numerical results on the scattering and absorption of an H-polarized plane by a single graphene strip in free space, including inclined incidence, can be found in [10]. The same paper contains accurate numerical study of the scattering by finite multi-strip graphene gratings using the Nystrom algorithm similar to the used here.

Figure 4 presents the total near-field patterns (i.e. the values of $|H_z|$) in four plasmon resonances P_s, $s = 1, 3, 5, 7$ marked in figure 3(b). Each of these plasmons can be interpreted as a Fabry–Perot-like standing wave, which is

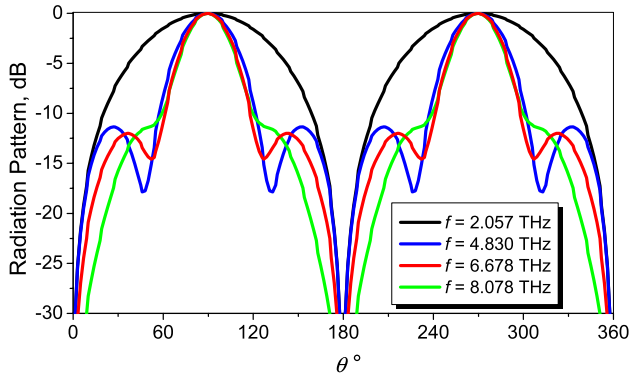

Figure 5. Normalized radiation patterns of the scattered field at the plasmon frequencies marked in figure 3(b).

formed by the reflections of the surface plasmon natural wave of a graphene layer from the strip edges. This wave has the propagation constant that can be found analytically using the GBC (1) as

$$\alpha_p = k\sqrt{1-(\sigma Z_0/2)^2}. \tag{14}$$

Then, following [16, 17], i.e. neglecting the losses and assuming for simplicity a zero reflection phase of such wave at the strip edge, the resonance frequencies can be found as roots of certain approximate characteristic equations. For the plasmon modes that are either even or odd with respect to the strip middle point, such equations can be cast to the common form as

$$\sin\left(\mathrm{Re}(\alpha_p)d\right) \approx 0, \tag{15}$$

that entails $\mathrm{Re}(\alpha_p)d \approx s\pi$, $s = 1, 2, 3, \ldots$. Then the corresponding natural frequencies are associated with the odd-index ($s = 1, 3, \ldots$) or even-index ($s = 2, 4, \ldots$) roots, respectively.

It is the wavelength of the mentioned plasmon surface wave (i.e. not the free-space wavelength) that becomes a characteristic length in the studied scattering problem. Note that only the odd-index plasmon resonances can be excited in the case of the normal incidence because of their modal field symmetry across the strip middle point, while the even-index plasmons remain dark modes in this case.

A wider-than-the-wavelength graphene strip behaves as an imperfect flat mirror that is visible in the far-field scattering patterns presented in figure 5. Indeed, at any frequency one can see two predominant lobes: the shadow lobe and the specularly reflected-wave lobe. If, however, the frequency approaches one of the surface plasmon frequencies one can observe the appearance of additional smaller lobes whose intensity depends on the quality factor of the corresponding plasmon resonance and whose number correlates with the index of the plasmon, i.e. with the number of the current variations along the strip width.

In contrast to the *H*-polarization, in the case of the *E*-polarized wave scattering no plasmon resonances appear. In figure 6, we present the dependences of the normalized TSCS versus the frequency (a) for the same strip and the chemical-potential values as in figure 3, and a sample total near-field pattern at $f = 3$ THz, and (b) for the graphene with $\mu_c = 1$ eV (green curve).

4. Micro-size graphene disk

4.1. Solution method: coupled dual IEs and method of analytical regularization

To solve the 3D scattering problem by a graphene disk, we use the method of dual IEs in the spectral domain together with the concept of analytical regularization [18]. We start by introducing the dimensionless (normalized to the radius of the disk) cylindrical coordinates (ρ, φ, ζ) with the origin at the disk center. The following expressions for the normal and tangential to the disk scattered field components in terms of the scalar and vector Fourier–Hankel transform can be written to satisfy the Maxwell equations and the condition of radiation

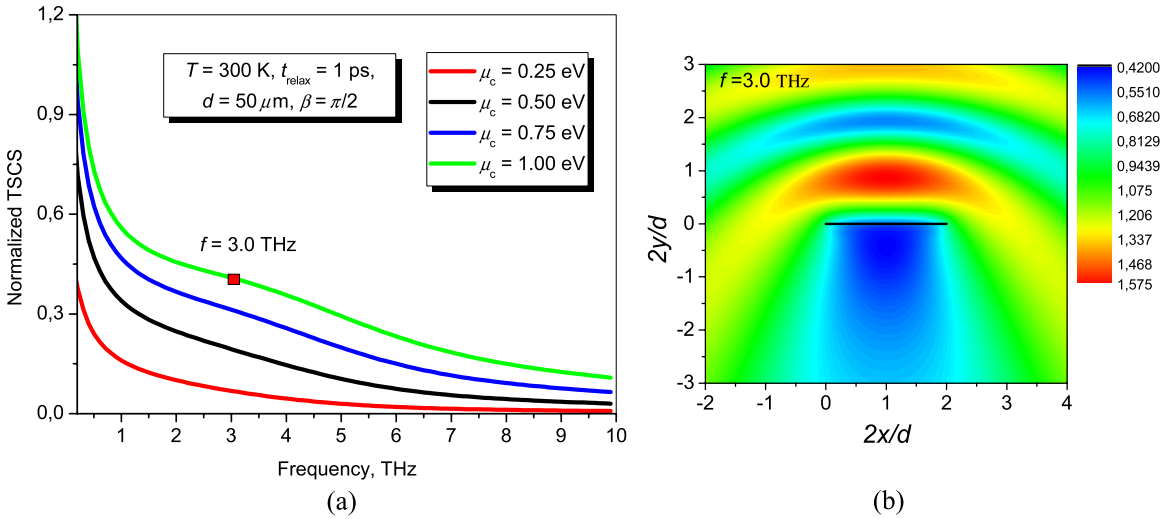

Figure 6. Normalized TSCS versus the frequency (a) and total near-field pattern at $f = 3$ THz (b) for a stand-alone graphene strip of $d = 50$ μm illuminated by a normally incident *E*-polarized plane wave.

at infinity:

$$\begin{pmatrix} E_z^{\mathrm{sc},\pm}(\rho,\varphi,\zeta) \\ Z_0 H_z^{\mathrm{sc},\pm}(\rho,\varphi,\zeta) \end{pmatrix} = \sum_{m=-\infty}^{\infty} \mathrm{e}^{\mathrm{i}m\varphi} \int_0^{\infty} \mathrm{e}^{\mathrm{i}\gamma(\kappa)|\zeta|} J_{|m|}(\kappa\rho) \times \begin{pmatrix} \kappa e_{m,z}^{\mathrm{sc},\pm}(\kappa) \\ \kappa h_{m,z}^{\mathrm{sc},\pm}(\kappa) \end{pmatrix} \mathrm{d}\kappa, \tag{16}$$

$$\begin{pmatrix} E_r^{\mathrm{sc},\pm}(\rho,\varphi,\zeta) \\ -\mathrm{i}E_\varphi^{\mathrm{sc},\pm}(\rho,\varphi,\zeta) \end{pmatrix} = \sum_{m=-\infty}^{\infty} \mathrm{e}^{\mathrm{i}m\varphi} \int_0^{\infty} \mathrm{e}^{\mathrm{i}\gamma(\kappa)|\zeta|} \bar{H}_m(\kappa\rho) \times \begin{pmatrix} \pm\mathrm{i}\gamma(\kappa) e_{m,z}^{\mathrm{sc},\pm}(\kappa) \\ -ka\, h_{m,z}^{\mathrm{sc},\pm}(\kappa) \end{pmatrix} \mathrm{d}\kappa \tag{17}$$

$$\begin{pmatrix} Z_0 H_r^{\mathrm{sc},\pm}(\rho,\varphi,\zeta) \\ -\mathrm{i}Z_0 H_\varphi^{\mathrm{sc},\pm}(\rho,\varphi,\zeta) \end{pmatrix} = \sum_{m=-\infty}^{\infty} \mathrm{e}^{\mathrm{i}m\varphi} \int_0^{\infty} \mathrm{e}^{\mathrm{i}\gamma(\kappa)|\zeta|} \bar{H}_m(\kappa\rho) \times \begin{pmatrix} \pm\mathrm{i}\gamma(\kappa) h_{m,z}^{\mathrm{sc},\pm}(\kappa) \\ ka\, e_{m,z}^{\mathrm{sc},\pm}(\kappa) \end{pmatrix} \mathrm{d}\kappa. \tag{18}$$

Here, Z_0 is the free-space impedance, $\gamma(\kappa) = [(ka)^2 - \kappa^2]^{1/2}$ is a complex-valued function with the branch corresponding to $\mathrm{Im}(\gamma(\kappa)) \geq 0$, k is the free-space wavenumber, and $\bar{H}_m(\kappa\rho)$ is the matrix kernel of the vector Hankel transform given by (see, for instance, [19])

$$\bar{H}_m(\kappa\rho) = \begin{pmatrix} J'_{|m|}(\kappa\rho) & mJ_{|m|}(\kappa\rho)/(\kappa\rho) \\ mJ_{|m|}(\kappa\rho)/(\kappa\rho) & J'_{|m|}(\kappa\rho) \end{pmatrix}. \tag{19}$$

Also, here J_m is the first-kind Bessel function of the order m, J'_m its first-order derivative, and $e_{m,z}^{\mathrm{sc},\pm}(\kappa)$ and $h_{m,z}^{\mathrm{sc},\pm}(\kappa)$ are the images of the field components normal to the disk in the spectral domain. By substituting expressions (17), (18) into the boundary conditions (1) we reduce the scattering problem to the following set of the coupled dual IEs for each azimuthal index:

$$\begin{cases} \displaystyle\int_0^{\infty} \bar{H}_m(\kappa\rho) \begin{pmatrix} \gamma(\kappa)\left(u_m^{\mathrm{sc},-}(\kappa) + u_m^{\mathrm{in},-}(\kappa)\right) + 2\,ka\,(Z_0\sigma)^{-1} u_m^{\mathrm{sc},-}(\kappa) \\ \mathrm{i}\,ka\left(v_m^{\mathrm{sc},+}(\kappa) + v_m^{\mathrm{in},+}(\kappa)\right) + 2\mathrm{i}\,(Z_0\sigma)^{-1}\gamma(\kappa) v_m^{\mathrm{sc},+}(\kappa) \end{pmatrix} \mathrm{d}\kappa = \bar{0} \qquad (\rho < 1) \\ \displaystyle\int_0^{\infty} \bar{H}_m(\kappa\rho) \begin{pmatrix} \mathrm{i}\,ka\, u_m^{\mathrm{sc},-}(\kappa) \\ -\gamma(\kappa) v_m^{\mathrm{sc},+}(\kappa) \end{pmatrix} \mathrm{d}\kappa = \bar{0} \qquad (\rho > 1), \end{cases} \tag{20}$$

where $u_m^{\mathrm{sc},\pm}(\kappa)$, $v_m^{\mathrm{sc},\pm}(\kappa)$ are the images of the jumps and the average values of the scattered field components normal to the disk, respectively. These are the functions to be found. Functions $u_m^{\mathrm{in},\pm}(\kappa)$ and $v_m^{\mathrm{in},\pm}(\kappa)$ are known and determined by the incident field.

To solve the obtained dual IEs (20) we follow the method of analytical regularization [18] and invert the most singular part (which is the static part) of the integral operators of IEs analytically. At the end of this procedure, we obtain the following set of coupled Fredholm second-kind IEs:

$$u_m^{\mathrm{sc},-}(\lambda) = \mathrm{i}\int_0^{\infty} \kappa^{-1} \left(\left(w(k) + \frac{2ka}{Z_0\sigma} \right) u_m^{\mathrm{sc},-}(\kappa) + \gamma(\kappa) u_m^{\mathrm{in},-}(\kappa) \right) S_{|m|-1/2}(\kappa,\lambda)\,\mathrm{d}\kappa - \mathrm{i}A_m^l \sqrt{2} \frac{\Gamma(|m|+1)}{\Gamma(|m|+1/2)} \frac{J_{|m|+1/2}(\lambda)}{\lambda^{1/2}}, \tag{21}$$

$$v_m^{\mathrm{sc},+}(\lambda) = -ka \frac{Z_0\sigma}{2} \frac{\lambda^{1/2}}{\gamma(\lambda)} \times \int_0^{\infty} \kappa^{-1/2} \times \left(v_m^{\mathrm{sc},+}(\kappa) + v_m^{\mathrm{in},+}(\kappa) \right) \times S_{|m|+1}(\kappa,\lambda)\,\mathrm{d}\kappa - 2mD_m^r \frac{J_{|m|}(\lambda)}{\gamma(\lambda)}, \tag{22}$$

$$A_m^l \frac{\Gamma(|m|+1)}{\Gamma(|m|+3/2)} - (ka)^{-1} 2D_m^r \frac{\Gamma(|m|+1/2)}{\Gamma(|m|)} = \sqrt{2}\int_0^{\infty} \kappa^{-3/2} \left(\left(w(\kappa) + \frac{2ka}{Z_0\sigma} \right) u_m^{\mathrm{sc},-}(\kappa) + \gamma(\kappa) u_m^{\mathrm{in},-}(\kappa) \right) J_{|m|+1/2}(\kappa)\,\mathrm{d}\kappa, \tag{23}$$

$$\mathrm{i}Z_0\sigma\,\mathrm{sgn}(m) A_m^l + \mathrm{sgn}(m) 2D_m^r = kaZ_0\sigma \int_0^{\infty} \kappa^{-1} \left(v_m^{\mathrm{sc},+}(\kappa) + v_m^{\mathrm{in},+}(\kappa) \right) J_{|m|}(\kappa)\,\mathrm{d}\kappa. \tag{24}$$

Here $w(\kappa) = \gamma(\kappa) - \mathrm{i}\kappa$, $\Gamma(x)$ is the Euler gamma function, and $S_\mu(\kappa,\lambda)$ is the smooth kernel function given by the integral and closed-form expressions as

$$S_\mu(\kappa,\lambda) = \kappa^{1/2}\lambda^{1/2} \int_0^1 J_\mu(\kappa\nu) J_\mu(\lambda\nu)\nu\,\mathrm{d}\nu = \frac{\kappa^{1/2}\lambda^{1/2}}{\kappa^2 - \lambda^2} \left(\lambda J_{\mu-1}(\lambda) J_\mu(\kappa) - \kappa J_{\mu-1}(\kappa) J_\mu(\lambda) \right). \tag{25}$$

The properties of the Fredholm second-kind IEs guarantee the existence and uniqueness of their solution, thus it is possible to use any reasonable analytical or numerical scheme to solve them. We use the numerical technique which is based on the truncation of the integration interval to the finite one combined with the discretization of the truncated equations using the Nystrom-type scheme [20]. Finally we obtain a set of linear algebraic equations and solve them numerically using the Gauss inversion of the corresponding matrix.

4.2. Numerical results and discussion

To study the excitation of the graphene-disk plasmon resonances by the point sources, we chose, as the figures-of-merit, the power radiated by the chosen source in the presence of the graphene disk and the power lost due to absorption. As a source we take one of two dipoles, namely a horizontal magnetic dipole and a vertical electric dipole. Both values will be normalized by the power radiated by the same source located in free space, $P_0 = (12\pi)^{-1} CI^2 (kg)^2$. Here the electric (magnetic) dipole case implies $C = Z_0$ ($C = 1/Z_0$) with I being the electric (magnetic) dipole current, and g is the dipole 'length,' so that Ig is electric (magnetic) dipole moment. Our aim is to study the excitation of the graphene plasmon resonances as the source of the incident field shifts from the disk axis toward the rim of the disk. We also analyze (similarly to the case of graphene strip) how the resonances shift if the chemical potential of graphene gets larger.

We start our consideration with the dipoles located on the disk axis ($r_0 = 0$) and change the chemical potential of

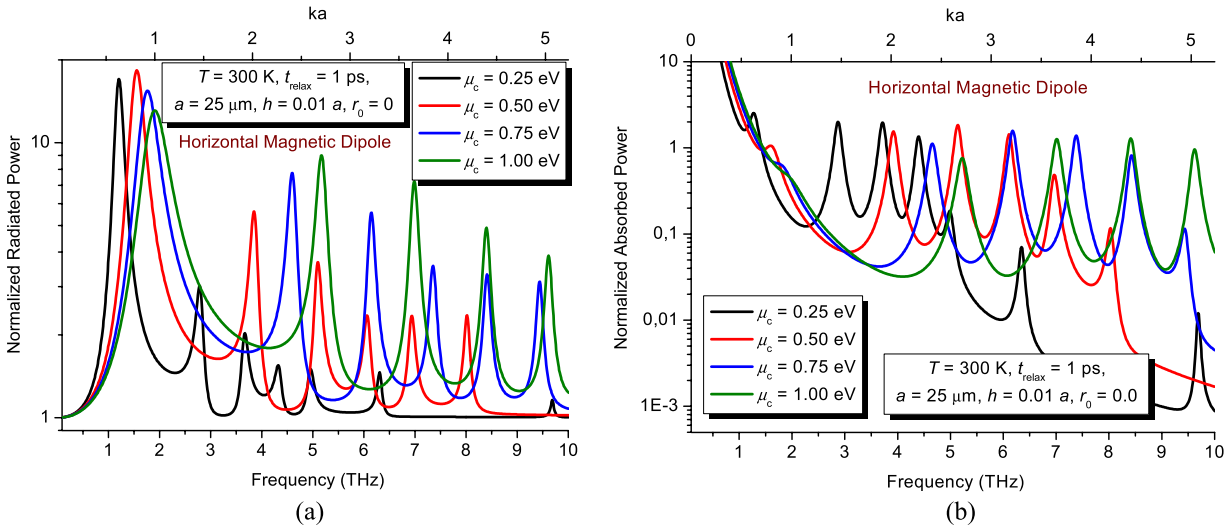

Figure 7. Normalized radiated and absorbed powers versus frequency for the graphene disk ($a = 25\ \mu$m) excited by the on-axis horizontal magnetic dipole.

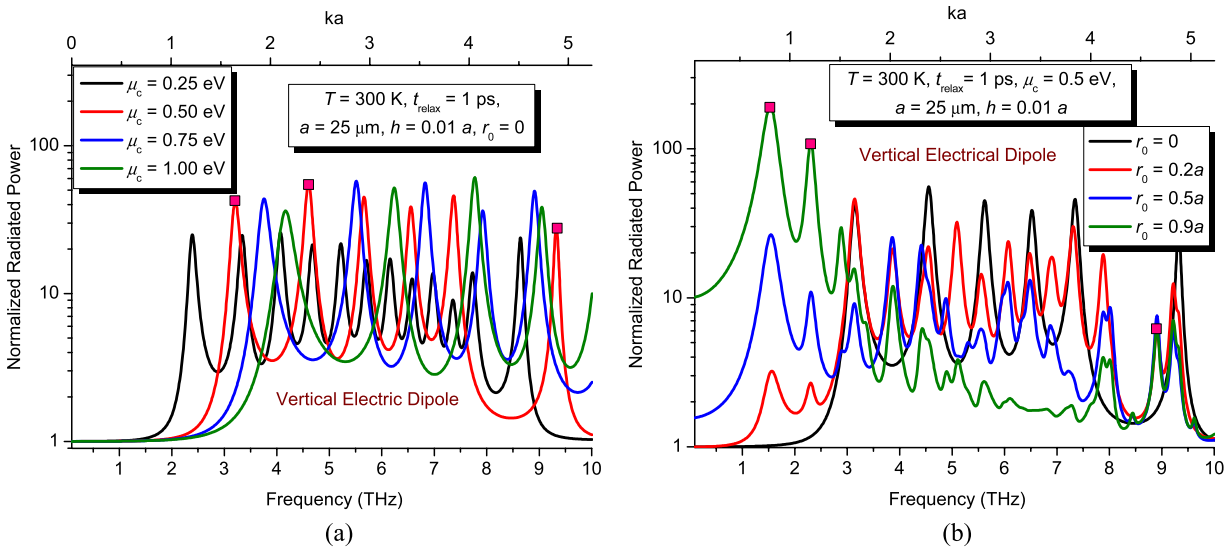

Figure 8. Normalized radiated powers versus frequency for the graphene disk ($a = 25\ \mu$m) excited by the on-axis (a) and the shifted (b) vertical electric dipoles.

the graphene ($\mu_c = 0.25;\ 0.5;\ 0.75;\ 1.0$ eV). Figure 7 shows the normalized radiated and absorbed powers as a function of the frequency in the case of horizontal magnetic dipole excitation.

One can see several resonance peaks on each curve. They correspond to the family of plasmon resonance modes with one variation of the field along the disk azimuth and several variations along the disk radius. Thus, for example, the resonance frequency $f = 1.5425$ THz for the red curve in figure 7(a) corresponds to the resonance mode with a single variation of the field along the azimuth (without variation along the radius). The typical far-field pattern in such resonance looks like the pattern in figure 9(d). Also note the up-shifting of the resonance frequency with increasing of the graphene chemical potential (this is the same as increasing the electrical bias of the graphene material).

Figure 8(a) shows frequency dependences of the normalized radiated power for the same parameters of graphene disk but in the case of the on-axis vertical electrical dipole excitation. Such incident field has no variations along the azimuth and thus it excites only azimuthally symmetric ($m = 0$) surface plasmon modes. Figures 9(a)–(c) show the radiation patterns at three resonance frequencies $f = 3.1368, 4.5512$ and 9.3182 THz for the red curve (which corresponds to the graphene chemical potential of 0.5 eV) in figure 8(a).

Figure 8(b) shows frequency dependences of the normalized radiated power for several different source-point locations. We start shifting the vertical electrical dipole from the axis of the disk to the rim and find excitation of plasmon modes of different azimuthal families ($m = 0, 1, 2, \ldots$).

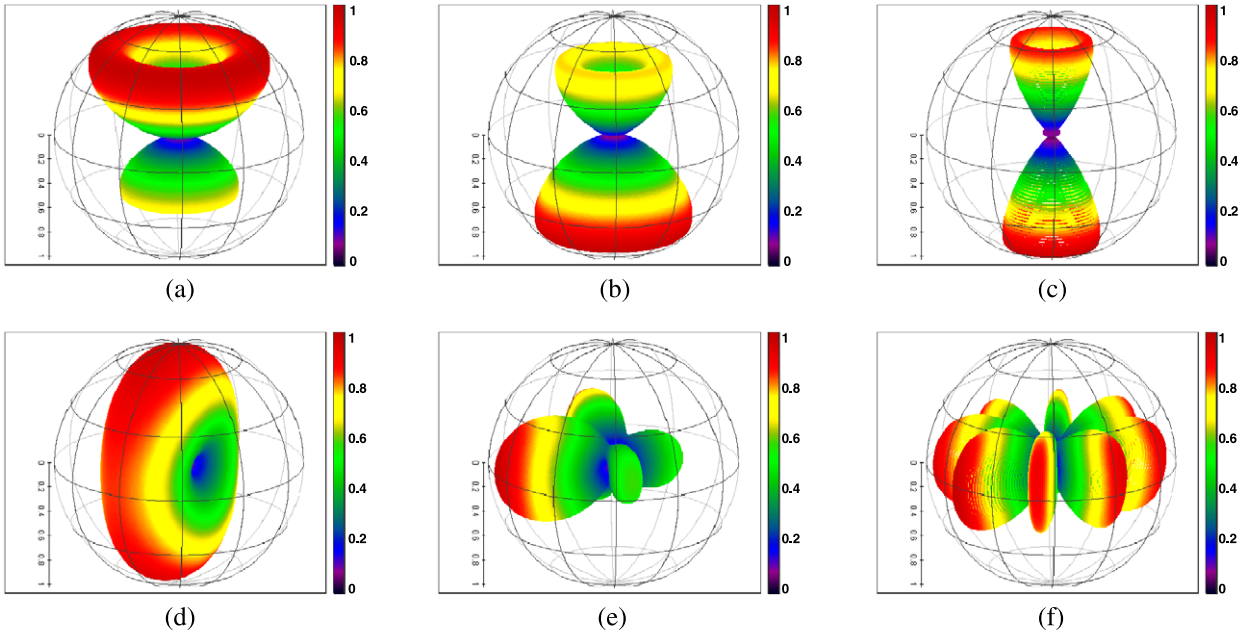

Figure 9. Far-field radiation patterns in the case of the graphene disk excited by the vertical electrical dipole; on-axis dipole location, $r_0 = 0; f = 3.1368$ THz (a), $f = 4.5512$ THz (b), $f = 9.3182$ THz (c) and shifted dipole location, $r_0 = 0.9a; f = 1.5425$ THz (d), $f = 2.3071$ THz (e), $f = 8.9016$ THz (f).

In line with the discussion in section 4.1 (see also [16, 17]), the plasmon resonance frequencies of graphene disk can be found from the approximate equation as follows:

$$J_m\left(\mathrm{Re}\left(\alpha_p\right)a\right) \approx 0, \qquad m = 0, 1, 2, \ldots \tag{26}$$

where α_p is given by (14).

The 3D far-field radiation patterns presented in figures 9(d)–(f) have been computed at three resonance frequencies $f = 1.5425$, 2.3071 and 8.9016 THz corresponding to the excitation of the plasmon modes with $m = 1, 2, 4$ and marked in figure 8(b).

5. Conclusions

We have presented two modeling methods and fast convergent numerical algorithms for the analysis of the excitation of the surface plasmon modes on a flat graphene strip and a flat graphene disk located in the free space. The modeling is based on the Maxwell equations and resistive-type boundary conditions on the strip or disk surface, where the graphene electron conductivity is included as a parameter. In the case of the graphene strip, the associated 2D scattering problem is reduced to a hyper-singular IE of the second type which we have solved using Nystrom-type discretization and the Chebyshev quadrature formulas. In the case of the graphene disk, the scattering problem is essentially a 3D one. It has been reduced to a set of coupled dual IEs for each azimuthal order (in the spectral domain) and further to the coupled pair of Fredholm second-kind IEs which we have solved numerically using the Nystrom-type discretization.

Using the above-presented computational instruments, we have studied the excitation of a graphene strip by the *H*- and *E*-polarized plane waves and a graphene disk by the elementary dipoles, horizontal magnetic and vertical electric. In each case we have computed the power characteristics such as scattering and absorption cross-sections and the radiated and absorbed powers, respectively. Our focus has been on the study of associated surface plasmon resonances of finite-size graphene scatterers. We have shown how the resonance frequencies shift for different values of the chemical potential of graphene material and visualized the near-zone and far-zone field patterns in the resonances of various types.

Acknowledgments

This work has been partially supported by the National Academy of Sciences of Ukraine via the State Target Program ‘Nanotechnologies and Nanomaterials’ and the European Science Foundation via the Research Networking Programme ‘Newfocus’. Many fruitful discussions with J S Gomez-Diaz, J Perruisseau-Carrier, J Mosig, A Vukovic and T M Benson are acknowledged with gratitude.

References

[1] Yan H, Li X, Chandra B, Tulevski G, Wu Y, Freitag M, Zhu W, Avouris P and Xia F 2012 Tunable infrared plasmonic devices using graphene/insulator stacks *Nature Nanotechnol.* **7** 330–4

[2] Nikitin A Y, Guinea F, Garcia-Vidal F J and Martin-Moreno L 2011 Edge and waveguide terahertz surface plasmon modes in graphene microribbons *Phys. Rev.* B **84** 161407(R)

[3] Tamagnone M, Gómez-Díaz J S, Mosig J R and Perruisseau-Carrier J 2012 Reconfigurable THz plasmonic antenna concept using a graphene stack *Appl. Phys. Lett.* **101** 214102

[4] Fallahi A and Perruisseau-Carrier J 2012 Design of tunable biperiodic graphene metasurfaces *Phys. Rev.* B **86** 195408
[5] Llatser I, Kremers C, Cabellos-Aparicio A, Jornet J M, Alarcón E and Chigrin D N 2012 Graphene-based nano-patch antenna for terahertz radiation *Photon. Nanostruct.–Fundam. Appl.* **10** 353–8
[6] Hanson G W 2008 Dyadic Green's functions for an anisotropic, non-local model of biased graphene *IEEE Trans. Antennas Propag.* **56** 747–57
[7] Geim K and Novoselov K S 2007 The rise of graphene *Nature Mater.* **6** 183–91
[8] Gusynin P, Sharapov S G and Carbotte J P 2007 Magnetooptical conductivity in graphene *J. Phys.: Condens. Matter* **19** 026222
[9] Han M Y, Oezyilmaz B, Zhang Y and Kim P 2007 Energy band gap engineering of graphene nanoribbons *Phys. Rev. Lett.* **98** 206805
[10] Shapoval O V, Gomez-Diaz J S, Perruisseau-Carrier J, Mosig J and Nosich A I 2013 Integral equation analysis of plane wave scattering by finite periodic gratings made of coplanar graphene strips in the THz frequency range *IEEE Trans. Terahz. Sci. Technol.* **3** 666–73
[11] Braver I M, Fridberg P S, Garb K L and Yakover I M 1988 The behavior of the electromagnetic field near the edge of a resistive half-plane *IEEE Trans. Antennas Propag.* **36** 1760–8
[12] Nosich A A and Gandel Y V 2007 Numerical analysis of quasi-optical multireflector antennas in 2D with the method of discrete singularities *IEEE Trans. Antennas Propag.* **55** 399–406
[13] Shapoval O V, Sauleau R and Nosich A I 2013 Modeling of plasmon resonances of multiple flat noble-metal nanostrips with a median-line integral equation technique *IEEE Trans. Nanotechnol.* **12** 442–9
[14] Gandel Y V and Kononenko A S 2006 Justification of the numerical solution of a hypersingular integral equation *Differ. Equ.* **42** 1326–33
[15] Tsalamengas J L 2006 Exponentially converging Nystrom's methods for systems of SIEs with applications to open/closed strip or slot-loaded 2D structures *IEEE Trans. Antennas Propag.* **54** 1549–58
[16] Filter R, Qi J, Rockstuhl C and Lederer F 2012 Circular optical nanoantennas: an analytical theory *Phys. Rev.* B **85** 125429
[17] Balaban M V, Sauleau R, Benson T M and Nosich A I 2011 Accurate quantification of the Purcell effect in the presence of a dielectric microdisk of nanoscale thickness *IET Micro Nano Lett.* **6** 393–6
[18] Balaban M V, Sauleau R, Benson T M and Nosich A I 2009 Dual integral equations technique in electromagnetic wave scattering by a thin disk *Prog. Electromag. Res.* B **16** 107–26
[19] Ali S and Kong J 1982 Vector Hankel transform analysis of annular-ring microstrip antenna *IEEE Trans. Antennas Propag.* **30** 637–44
[20] Balaban M V, Smotrova E I, Shapoval O V, Bulygin V S and Nosich A I 2012 Nystrom-type techniques for solving electromagnetics integral equations with smooth and singular kernels *Int. J. Numer. Modelling, Electron. Netw. Devices Fields* **25** 490–511